JGR Space Physics

RESEARCH ARTICLE
10.1029/2021JA030004

Space-Ground Observations of Dynamics of Substorm Onset Beads

Y. Nishimura[1], A. V. Artemyev[2,3], L. R. Lyons[4], C. Gabrielse[5], E. F. Donovan[6], and V. Angelopoulos[2]

[1]Department of Electrical and Computer Engineering and Center for Space Physics, Boston University, Boston, MA, USA, [2]Department of Earth, Planetary, and Space Sciences, University of California, Los Angeles, CA, USA, [3]Space Research Institute of Russian Academy of Sciences, Moscow, Russia, [4]Department of Atmospheric and Oceanic Sciences, University of California, Los Angeles, CA, USA, [5]The Aerospace Corporation, Los Angeles, CA, USA, [6]Department of Physics and Astronomy, University of Calgary, Calgary, Alberta, Canada

Key Points:

- Duskward beads are related to energetic ion drift. The duskward $E \times B$ and electron drifts reduced the cross-tail current at onset
- Dawnward beads are related to $E \times B$ and electron drifts. The duskward ion drift and tail current were reduced at onset
- Species involved in bead propagation changes with the electric field. Tail current reduction by enhanced $E \times B$ destabilizes the plasma sheet

Supporting Information:

Supporting Information may be found in the online version of this article.

Correspondence to:

Y. Nishimura,
toshi16@bu.edu

Citation:

Nishimura, Y., Artemyev, A. V., Lyons, L. R., Gabrielse, C., Donovan, E. F., & Angelopoulos, V. (2022). Space-ground observations of dynamics of substorm onset beads. *Journal of Geophysical Research: Space Physics*, *127*, e2021JA030004. https://doi.org/10.1029/2021JA030004

Received 29 SEP 2021
Accepted 13 JAN 2022

Author Contributions:

Conceptualization: Y. Nishimura
Data curation: E. F. Donovan, V. Angelopoulos
Formal analysis: Y. Nishimura
Funding acquisition: Y. Nishimura, L. R. Lyons, C. Gabrielse, E. F. Donovan, V. Angelopoulos
Investigation: Y. Nishimura, A. V. Artemyev, C. Gabrielse
Methodology: Y. Nishimura, A. V. Artemyev
Project Administration: Y. Nishimura
Resources: E. F. Donovan, V. Angelopoulos
Software: Y. Nishimura, A. V. Artemyev, E. F. Donovan, V. Angelopoulos
Supervision: Y. Nishimura
Validation: Y. Nishimura, L. R. Lyons
Visualization: Y. Nishimura

Abstract We present observations during two substorms using simultaneous Time History of Events and Macroscale Interactions During Substorms satellites and all-sky imagers to determine plasma sheet dynamics associated with substorm auroral onset beads. The multi-satellite observations showed that the cross-tail current decreased and the field-aligned currents increased at the substorm auroral onset, indicating that the satellites detected an initiation of the currents being deflected to the ionosphere. For duskward-propagating beads, the electric field was tailward, and ions were accumulated closer to the Earth than electrons. The mapped bead propagation speed was close to energetic ion drift speed. The $E \times B$ and electron drift speeds increased duskward and reduced the cross-tail current at the onset. For dawnward-propagating beads, the electric field was equatorward/earthward, and electrons were inferred to accumulate earthward of ions. The mapped bead propagation speed was comparable to the dawnward $E \times B$ and electron drift speeds. The duskward ion drift and tail current were reduced, and electrons became the dominant current carrier. We suggest that the plasma species that is responsible for the bead propagation changes with the electric field configuration and that the tail current reduction by the enhanced $E \times B$ drift at onset destabilizes the plasma sheet. Ion and electron outflows substantially increased low-energy plasma density and may have increased the role of $E \times B$ drifts. The bead wavelength was comparable to ion gyroradius and thus ion kinetic effects are important for determining the wavelength. In the dawnward-propagating event, the mode of oscillation in the plasma sheet was suggested to be the sausage-mode flapping oscillations.

Plain Language Summary Aurora in the night sky often begins with a sudden intensification called substorms, and the auroral intensification shows a wave-like display (beads). It is critical to understand the origin of beads for revealing the mechanism of the sudden auroral intensifications, but it has been extremely difficult to find satellite observations in space to explore the magnetospheric source region of substorms. We identified two simultaneous observations of auroral beads at the beginning substorm auroral intensification by all-sky imagers and related plasma dynamics by the Time History of Events and Macroscale Interactions During Substorms satellites in the plasma sheet. We found that the bead structure and propagation are related to charge accumulation and fast plasma streams in the plasma sheet. The plasma flow speed coincided with the bead speed, and the charge distribution and plasma stream direction reversed when the auroral beads moved to an opposite direction, giving strong evidence of the connection between the observations at the two locations. The plasma streams reduced the electric currents in the plasma sheet, and we suggest that the current reduction destabilizes the plasma sheet and initiates the substorm auroral intensification.

1. Introduction

Substorm auroral onset is characterized by an initial brightening along an auroral arc in the equatorward portion of the nightside auroral oval, and the initial brightening involves ray structures during the first few minutes after the onset (Akasofu, 1964). The rays are also called beads, and they are considered to be the auroral manifestation of wave instability in the near-Earth plasma sheet at substorm onset (Donovan et al., 2006). Case studies (Chang & Cheng, 2015; Gallardo-Lacourt et al., 2014; Henderson, 2009; Liang et al., 2008; Motoba et al., 2012; Rae et al., 2010; Sakaguchi et al., 2009) and statistical analyses (Kalmoni et al., 2018; Nishimura et al., 2016) have documented key properties of beads: Beads commonly occur associated with substorm auroral onset, and

Writing – original draft: Y. Nishimura
Writing – review & editing: A. V. Artemyev, L. R. Lyons

auroral intensity of beads grows exponentially. The wavelength along the onset arc is typically 50–130 km in the ionosphere, and beads propagate along the arc at a few km/s. The propagation direction of beads, however, is not always the same. Dawnward (eastward) propagation is most frequently observed, but beads can also propagate duskward (westward) or in both directions. The wave period at a fixed location is a few tens of seconds, and ground magnetometers near onset arcs show magnetic field fluctuations at a similar period. Beads are also associated with ionospheric flow shears that indicate alternating upward and downward field-aligned currents.

Beads are distinguished from pre-onset auroral waves that are sometimes present along substorm growth-phase arcs (Uritsky et al., 2009). Pre-onset waves are much fainter than beads, and their amplitude does not increase over time. At substorm auroral onset, pre-onset waves intensify suddenly and become beads, indicating that pre-onset waves are a precursor of onset beads (Nishimura et al., 2014). The magnetotail counterpart of pre-onset waves can be characterized by oscillations of the magnetic field and radial electron velocity, and they are suggested to be caused by kinetic ballooning/interchange instability (BICI) (Panov et al., 2012). Bead-like auroral structures can also occur during other types of auroral intensifications, and they have also been attributed to BICI (Panov et al., 2019).

In contrast, in-situ observations associated with substorm onset beads have not been reported to date, because it is extremely rare to have satellite observations in the plasma sheet in the possible onset region during the short lifetime of beads that are measured by auroral imagers. Observationally, it is not understood what plasma sheet structures are associated with the beads, and what determines the direction and speed of beads. A number of satellite observations have revealed the presence of quasi-periodic oscillations of the magnetic field in the near-Earth plasma sheet associated with substorms (Le Contel et al., 2000; Lui, 1996; Pu et al., 1997; Ohtani et al., 1998; Roux et al., 1991; Saito et al., 2008; Shiokawa et al., 2005). However, it has been difficult to identify whether and how they are related to substorm onset and auroral beads because it is difficult to confirm that substorm auroral onset and beads were detected simultaneously with the satellite observations. Without observations of beads, it is not possible to identify whether the observed features correspond to beads or arise from other types of activities during substorms. In addition, similarities and differences between ion and electron dynamics at substorm onset have rarely been investigated. Examination of kinetic features is important to address the substorm onset beads problems because the bead wavelength mapped to the plasma sheet is comparable to the ion gyroradius. The duskward and dawnward bead propagations also suggest that the propagation is not solely governed by a drift of a single plasma species, but that electric field structures or the key plasma species change between substorms.

The purpose of the present study is to determine what structures in the near-Earth plasma sheet are associated with substorm onset beads. Particularly, we will identify what are the magnetotail counterpart of the duskward and dawnward propagation of beads. We selected two substorm events that were detected by the Time History of Events and Macroscale Interactions During Substorms (THEMIS) all-sky imagers (ASIs) (Mende et al., 2008) in conjunction with the THEMIS satellites (Angelopoulos, 2008) in the plasma sheet. The substorm auroral onset was identified as a sudden auroral brightening that occurred in the equatorward portion of the auroral oval within one of the ASI fields-of-view (FOV), followed by poleward expansion (Akasofu, 1964). In order to remove pseudo-breakup, we required that the H-component of the ground magnetic field near the substorm onset location decreased by more than 200 nT. We did not require that the substorm be isolated but required that there was no auroral intensification or electrojet enhancement for 30 min prior to the substorm onset. At least one of the THEMIS satellites should be located in the central plasma sheet ($\beta > 1$), and its footprint (calculated by the T96; Tsyganenko, [1995]; magnetic field model) should be within the magnetic local time (MLT) range of the substom auroral onset beads. Because the precise mapping location is not known, the criteria on the satellite location only identify potential conjunctions. The presence of plasma and magnetic field variations at substorm onset at the satellite location is used to evaluate whether the satellite is in the region of substorm onset in the plasma sheet.

2. Results

2.1. Duskward Propagation

2.1.1. Ground-Based and Multi-Satellite Observations

Figure 1a shows an auroral keogram at Yellow Knife (YKNF) in the pre-midnight sector for a substorm on 29 March 2008. The auroral oval slowly moved equatorward before ~06:50 UT, and then a sudden auroral brightening started in the equatorward portion of the auroral oval at ~06:50 UT. This brightening was followed by

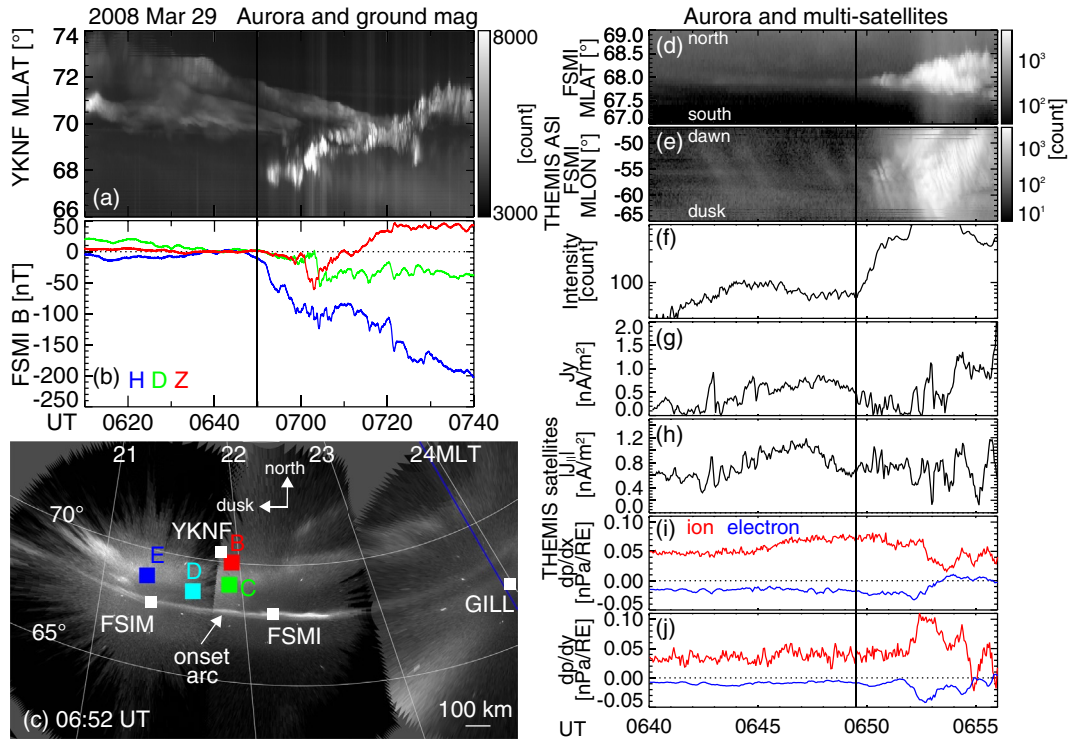

Figure 1. The left column shows (a) a north-south keogram near the central meridian of the Yellow Knife (YKNF) Time History of Events and Macroscale Interactions During Substorms (THEMIS) all-sky imagers (ASI), (b) ground magnetometer data at Fort Smith (FSMI), and (c) THEMIS ASI snapshot at 06:52 UT during the substorm on 29 March 2008. The THEMIS satellite footprints using the T96 field model are shown as the colored dots. The right column shows (d) the north-south keogram near the central meridian of the FSMI ASI, (e) east-west keogram along the onset arc (68.0° magnetic latitude) from the FSMI ASI, (f) auroral intensity on the onset arc at −60° magnetic longitude, (g) duskward cross-tail current density and (h) field aligned centres magnitude calculated from THEMIS B, C, D, and E, and (i) sunward and (j) duskward pressure gradients (red: ion, blue: electron) from THEMIS C, D, and E. The vertical line marks the substorm auroral onset time.

a prolonged poleward expansion that reached beyond the preceding auroral poleward boundary latitude. The *H*-component of the ground magnetic field at Fort Smith (FSMI) near the arc decreased by ∼200 nT associated with the arc brightening (Figure 1b), which is a typical signature of the substorm auroral electrojet. Thus the initiation of the auroral brightening is a substorm auroral onset, and the poleward expansion corresponds to the substorm expansion phase (Akasofu, 1964). The equatorward motion of the auroral oval before the onset is the growth phase, and the auroral oval was quiet for more than an hour prior to the onset.

As shown in the ASI snapshot right after the onset at 06:52 UT (Figure 1c), the auroral onset was fully covered by the THEMIS ASI FOV near the zenith of the FSMI and Fort Simpson (FSIM) ASIs, and the onset arc showed a wave-like luminosity modulation (beads; hereinafter referred to as onset waves). The T96 footprints of THEMIS-B, C, D, and E were located within the MLT range of the onset waves. The THEMIS satellites were located to the dusk of the brightest location of the onset arc. However, this shift does not affect the comparison of the two events in our work, because the THEMIS satellites in the second event were also to the dusk of the emission peak. The footprints were slightly poleward of the onset arc latitude, but footprint latitudes are sensitive to the degree of the magnetic field stretching in the model, which tends to have large uncertainties. Thus we did not require that the satellite footprints were located on the onset arc.

Figures 1d and 1e present a north-south keogram across the onset arc and an east-west keogram along the onset arc in the FSMI ASI at 06:40-06:56 UT. The line plot in Figure 1f depicts auroral luminosity on the onset arc in the western portion of the FSMI ASI FOV (68° magnetic latitude (MLAT) and −60° magnetic longitude (MLON)). The growth-phase arc was located at 68° MLAT, and the arc had faint pre-onset waves that propagated duskward (weak luminosity structures moving toward higher longitudes in Figure 1e). Then the luminosity increased exponentially starting at 06:49:30 UT (auroral onset). In the early expansion phase, the onset arc was

dominated by auroral onset waves that propagated duskward with a period of a few tens of seconds (based on the luminosity at a fixed longitude in Figure 1e).

The rest of the panels in Figure 1 shows data products that were derived from the multiple THEMIS satellites. The curlometer technique (Artemyev, Angelopoulos, Runov, & Petrokovich, 2016; Dunlop et al., 2002) using magnetic field observations by THEMIS-B, C, D, and E provided the tail current (Figure 1g) and field-aligned current (FAC, Figure 1h) that flowed through the region surrounded by the four satellites. The earthward (Figure 1i) and duskward (Figure 1j) pressure gradients (red: ion, blue: electron) were calculated from the equatorial pressure at THEMIS-C, D, and E (Artemyev et al., 2019). The magnetic field, pressure, and location of each satellite are given in Figure S1 in Supporting Information S1. Note that the currents and pressure gradients are only considered as representative values at the scale of the satellite separations. The currents and pressure gradients may have structures smaller than the satellite separations, but these methods cannot resolve such structures. The large spacecraft separation and non-ideal four spacecraft configuration (see discussion in Artemyev et al. [2019]) did not allow precise calculation of current density magnitude, but current variations would be reliable. $|\nabla \cdot \boldsymbol{B}|/|\nabla \times \boldsymbol{B}|$ was generally less than one (not shown).

The duskward cross-tail current, FAC, and earthward ion pressure gradient slowly increased during the growth phase until ~06:47 UT. The cross-tail current enhancements indicate a thinning of the plasma sheet, which is a typical signature of the growth phase (Artemyev, Angelopoulos, Runov, & Petrokovich, 2016; Petrukovich et al., 2013; Sergeev et al., 2011). The earthward ion pressure gradient is generally expected in the plasma sheet (e.g., Yue et al., 2015). The duskward ion pressure gradient in Figure 1j indicates that the satellites were located dawnward of an ion pressure peak, where upward FACs mapping to the growth phase arc were expected (Yang et al., 2013). The earthward ion pressure gradient became steady and the currents decreased at 06:47-06:49:30 UT. The increase and subsequent decrease in the FAC at the THEMIS observation region is analogous to the luminosity change of the growth phase arc (Figure 1f), although the peak time has a ~2-min difference. The magnetic field at THEMIS-C, D, and E had quasi-periodic oscillations of a few tens of seconds (Figures S1 in Supporting Information S1), and they correspond to quasi-periodic modulation of the cross-tail current and FAC. The quasi-periodic oscillations would correspond to the pre-onset auroral waves along the growth phase arc. These similarities indicate that the THEMIS satellites were located in a region that maps to the growth phase arc. At the substorm onset, the cross-tail current suddenly decreased and the FAC slightly increased. The reduced tail current, enhanced FAC, and auroral intensification at the substorm onset suggests that part of the tail current closed through the ionosphere as expected from the wedge-type current system (e.g., Boström, 1964) and that the satellites covered the region of substorm onset. The earthward ion pressure gradient decreased further a few minutes after the onset, and it coincided with the beginning of the larger auroral intensification and poleward expansion. The FAC increase was small, and the FAC after the onset was less than the largest FAC in the growth phase. This could be because the FAC was localized and could not be resolved well by the curlometer technique.

Interestingly, the electron pressure gradient was directed tailward and dawnward, which was opposite to the ion pressure gradient (Figures 1i and 1j). It means that the ions and electrons did not have the same pressure distributions but followed different transport processes, likely because ions are not fully magnetized but electrons are mostly magnetized in the thin current sheet (Pritchett & Coroniti, 2013). Considering the quasi-neutrality of the magnetotail plasma, differences in ion and electron pressure distributions should be attributed mainly to differences in temperature distribution (Artemyev, Angelopoulos, Runov, & Zelenyi, 2016). Similarities and differences between ions and electrons as well as their implications to the substorm onset processes are investigated further in the later sections.

2.1.2. THEMIS-D Observations: Moments

THEMIS-D was closest to the neutral sheet and thus we present THEMIS-D observations in detail. Figures 2c and 2d show that B_z is much larger than $|B_x|$, and plasma β was very high (27.5 at the auroral onset). Thus the satellite was well within the central plasma sheet. After the auroral onset, THEMIS-D detected enhancements of B_z, v_x (Figures 2e and 2f, more noticeably in electrons than ions), and energetic ion and electron fluxes (Figures 2g and 2h). Those are typical signatures of dipolarization flux bundles (DFBs) (Liu et al., 2014), and thus the satellite was in the longitude range of enhanced earthward transport during the substorm expansion phase. The magnetic field and velocities also had quasi-periodic oscillations. THEMIS-E was located just to the west of THEMIS-D and detected nearly identical features.

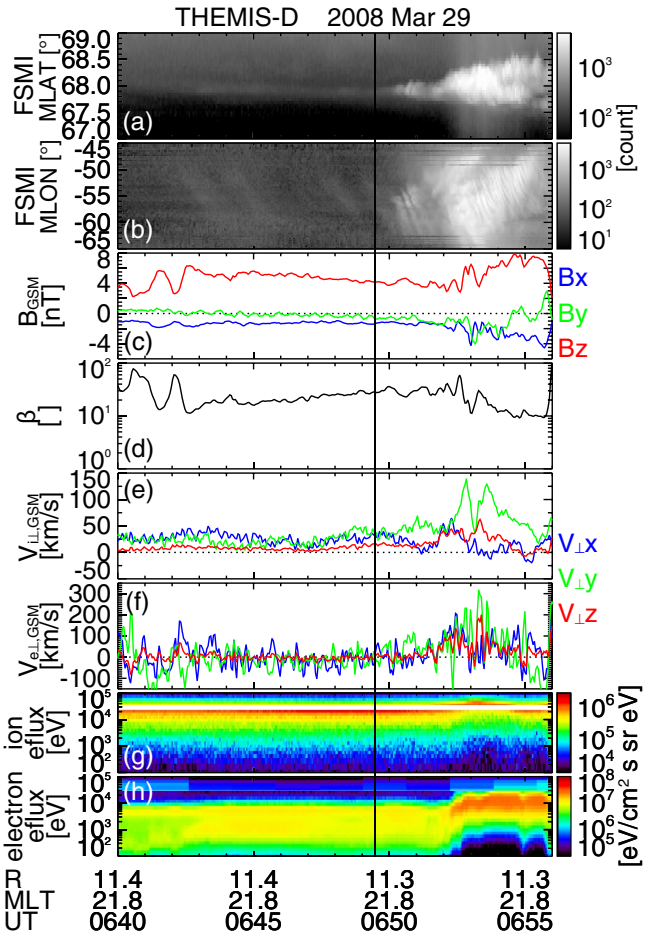

Figure 2. (a) The north-south keogram from the Fort Smith (FSMI) all-sky imagers (ASI), (b) east-west keogram along the onset arc from the FSMI ASI, and Time History of Events and Macroscale Interactions During Substorms -D satellite observations of (c) the magnetic field, (d) β, (e) $v_{i\perp}$, (f) $v_{e\perp}$, (g) ion energy flux, and (h) electron energy flux. The moments combine data from the electrostatic analyzer and solid state telescope instruments. β includes both ion and electron pressures (Baumjohann et al., 1990). Data over a wider time span and additional parameters (density, temperature, and pressure) are shown in Figure S2 in Supporting Information S1.

Figure 3c compares the dawn-dusk component of the ion (red), electron (blue), and $E \times B$ (black) velocities. The 3-day electric field vectors (Figure 3b) were obtained from the two measured components on the satellite spin plane from the Electric Field Instrument and the spin-axis electric field using $E \cdot B = 0$, which is a reasonable assumption in the plasma sheet for DC electric field. Before the substorm auroral onset, the ion velocity was duskward and increased further toward the auroral onset time, while the $E \times B$ velocity fluctuated around zero. The electron velocity was slightly dawnward. The difference between the ion and $E \times B$ velocities indicates that the duskward ion velocity corresponds to ion diamagnetic drift as expected from the earthward ion pressure gradient. After the substorm onset, the electron velocity increased to ~200–300 km/s and remained close to the $E \times B$ speed, while the ion velocity only increased to ~120 km/s. Because the earthward ion pressure gradient decreased after the onset (Figure 1i), the velocity increase does not simply reflect changes in the diamagnetic drift speed. The velocity increase likely involves ion energization after the onset (Figure 2g), where energetic ion fluxes increased and low-energy ion fluxes decreased. As shown later, the duskward speed of energetic ions increased after the onset. A combination of the magnetic drift of energetic ions and a small contribution of $E \times B$ drift of low-energy ions would explain the ion velocity enhancement that is smaller than the $E \times B$ speed.

Interestingly, the electrons drifted duskward after the onset in this event, as opposed to the dawnward magnetic drift direction. The duskward $E \times B$ drift was associated with a tailward electric field (Figure 3b). The tailward electric field was initially weak and then became large as the dipolarization front developed. The presence of the tailward electric field suggests that ions were accumulated closer to the Earth than electrons, and a small charge separation creates the polarization electron field. Such a tailward electric field is known as Hall electric field and is typical in the near-Earth current sheet (Artemyev, Angelopoulos, Runov, & Zelenyi, 2016).

The large duskward electron velocity has a significant impact on modifying the cross-tail current because the duskward-drifting electrons carry a dawnward current that reduces the cross-tail current. Figure 3d shows the cross-tail current densities carried by ions (red, $en_i v_{i,y}$) and electrons (blue, $-en_e v_{e,y}$). The net current density (gray, sum of the ion and electron currents) and its 1-min running average (black) are shown in Figure 3e. This method has been shown to provide reasonable currents when the bulk of the plasma population is detected (Artemyev et al., 2017). Before the onset, the electron current oscillated near zero, and the ion current was duskward. Thus the duskward cross-tail current during the growth phase was mostly carried by the ions. Around the time of the onset, the dawnward electron current increased to ~2 nA/m^2, while the duskward ion current only slightly increased. As a consequence, the net cross-tail current nearly vanished. This cross-tail current reduction is consistent with the current reduction obtained by the curlometer technique (Figure 1g), and provides an explanation that the duskward drifting electrons by $E \times B$ reduced the current. The reduction of the cross-tail current would weaken the magnetic field stretching in the magnetotail and may contribute to destabilize the plasma sheet including the formation of the dipolarization (Figure 2c) in the beginning of the substorm expansion phase.

In the quasi-steady plasma sheet, the duskward drift of plasma sheet ions is related to the diamagnetic drift (Wang et al., 2004), while the electron drift is related to the $E \times B$ drift by the equatorward (and earthward) electric field (Hesse et al., 1998; Lu et al., 2018; Zelenyi et al., 2010). The dawnward diamagnetic drift speed of electrons is much smaller (~20%) than the duskward ion diamagnetic drift speed (Miyashita et al., 2020). While this event is overall consistent with their findings, a major difference is that the electric field was directed tailward (or poleward at off-equatorial locations) and the $E \times B$ drift was duskward. The duskward electron drift substantially

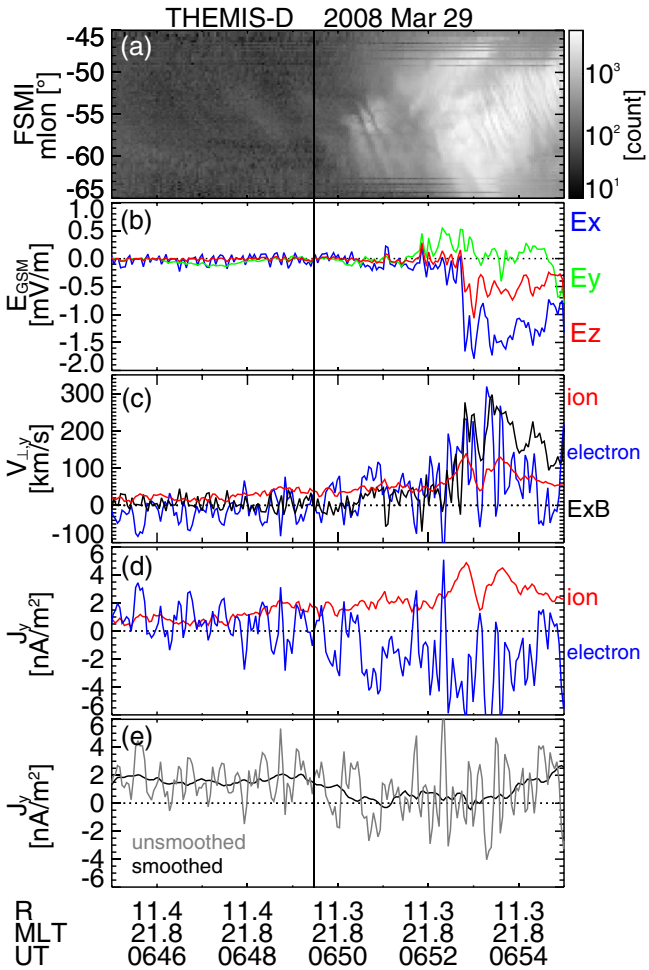

Figure 3. (a) The east-west keogram along the onset arc from the Forth Smith all sky imagers, (b) electric field, (c) duskward velocities (red: ion, blue: electron, black: $E \times B$), (d) duskward current densities (red: ion, blue: electron), and (e) net duskward current density (gray: unfiltered, black: 60-s smoothed).

reduced the cross-tail current. The reduced current could contribute to disturbing the force balance in the near-Earth magnetotail and could enhance the substorm instability.

Figure 4 shows the east-west keogram, the high-pass filtered auroral intensity at −56.5° MLON, dawn-dusk velocities, and high-pass filtered magnetic field and pressures. The high-pass filtering used a 60-s cut-off period to extract modulations that are comparable to the onset wave period (a few tens of seconds). Figures 4d and 4e show the dawn-dusk ion and electron velocity moments (from Figure 3c) as black lines, and partial velocity moments for the plasma sheet (magenta) and low-energy (cyan) populations. The partial velocity moments in this event were only available every 96 s, and they are not suitable to investigate rapid temporal variations. They are, however, useful for evaluating the energy dependence of the drift speeds. The duskward drift speed of the low-energy ion velocity (cyan in Figure 4d) increased and stayed close to the total velocity moment. The duskward velocity of the plasma sheet ions (magenta in Figure 4d) also increased and was larger than the total velocity moment throughout this time interval. None of the ion velocities closely followed the $E \times B$ velocity likely because the ions were not fully magnetized. Both plasma sheet and low-energy electrons followed the electron bulk flow velocity (close to the $E \times B$ velocity). These comparisons support the suggestion that the electrons followed the $E \times B$ drift, while the plasma sheet ions were affected by both diamagnetic and $E \times B$ drifts.

We traced each luminosity enhancement of the onset waves as shown by dashed lines in Figure 4a, and calculated that the duskward propagation speed was in a range of 7.1–10.6 km/s (0.17–0.25 deg/s) in the ionosphere at 110 km altitude, which is a typical mapping altitude for several keV electron precipitations. This range of speed corresponds to 170–240 km/s at the THEMIS-D location based on the T96 model, although the calculation using the model magnetic field should be considered as a rough estimate at best. This range of speed is shown as gray lines in Figures 4c–4e.

While none of the velocity moments perfectly matched the duskward velocity of the auroral onset waves mapped to the THEMIS-D location, the plasma sheet ion velocity was overall the closest to the mapped onset wave velocity. The plasma sheet ion velocity was slightly slower than the mapped onset wave velocity until ~06:52 UT and then it became slightly larger than the mapped onset wave velocity. The $E \times B$ and electron drift velocities also became comparable to the mapped onset wave velocity after ~06:52 UT, but those velocities were nearly zero until ~06:52 UT and cannot explain the onset wave velocity during the first few minutes. This observation supports the kinetic simulation by Pritchett and Coroniti (2013), where the duskward wave propagation is related to the duskward ion drift speed. The velocities at THEMIS-E were comparable to those at THEMIS-D (not shown). The velocity enhancements at THEMIS-E occurred within a few tens of seconds from THEMIS-D, and the time lag is consistent with westward signal propagation at a few hundred km/s speed.

The velocities had quasi-periodic oscillations, and the velocity oscillations had a similar period to the auroral intensity at a fixed location (Figure 4b). The real magnetic footprint location is not known and would not be fixed to a longitude. Thus, we do not expect that the auroral intensity correlates perfectly with the parameters measured by the satellites. However, the presence of the oscillations in aurora and in-situ velocities supports that the satellites in the near-Earth plasma sheet were magnetically connected to the onset waves and that the velocity modulation was related to the onset waves. The magnetic field also had quasi-periodic oscillations (Figure 4f), indicating that modulation of the current density perturbed the magnetic field. Total pressure variations were dominated by the ion pressure term until ~06:50 UT, and then the electron and magnetic pressure terms contributed more to the total pressure variations (Figure 4g). The pressure observations also support that electron dynamics became

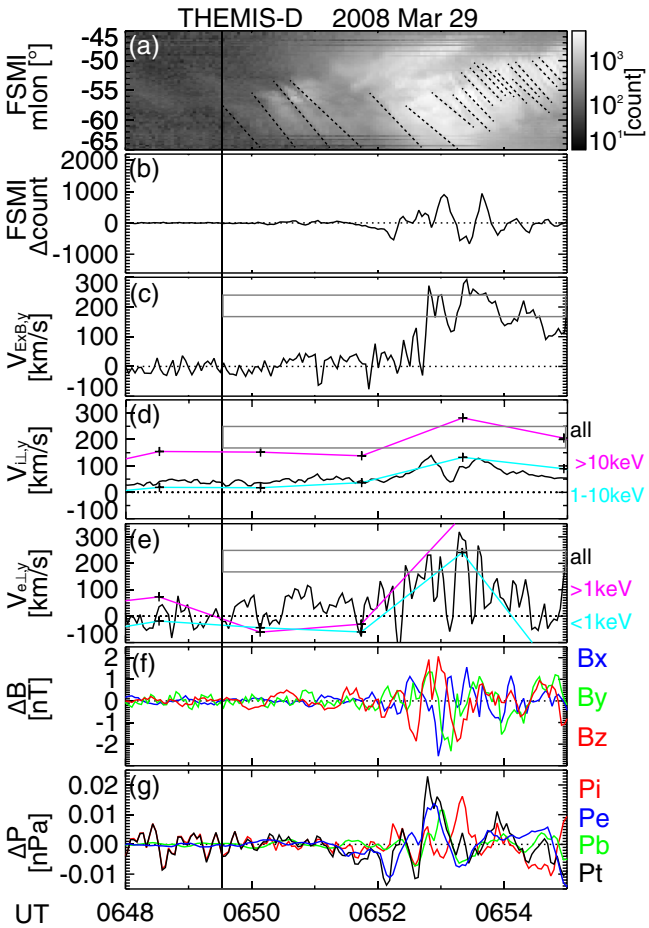

Figure 4. (a) The east-west keogram along the onset arc from the Forth Smith all-sky imager, (b) a line plot of the detrended auroral intensity at −56.5° magnetic longitude, and Time History of Events and Macroscale Interactions During Substorms -D satellite observations of (c) duskward $E \times B$ speed, (d) $v_{i\perp,y}$, and (e) $v_{e\perp,y}$, (f) the detrended magnetic field, (g) detrended pressures (red: ion, blue: electron, green: magnetic, black: total). The magenta and cyan lines in Panels d–e show partial velocity moments for plasma above and below 10 (ion) and 1 (electron) keV when distribution function data are available. The detrending used a 60-s cut-off period. The dashed lines in Panel a trace major onset waves. The gray lines in Panel c–e show the upper and lower velocities of onset waves mapped to the plasma sheet.

important after the onset. The pressure variations, however, had somewhat longer periods than that of the onset waves and were not correlated with the electron velocity or auroral intensity.

The azimuthal wavelength of the onset waves during the first few minutes after the onset is ∼70–120 km (1.7°–2.9° MLON) in the ionosphere (Figure 4a), and this range roughly maps to ∼2,000–3,600 km in the magnetotail (the size of each auroral intensity enhancement is half the wavelength). This range corresponds to the gyroradii of ∼5–15 keV ions in the 5 nT magnetic fields, which are near the energy with the peak ion energy flux (Figure 2g). Although the electron drift was suggested to play a key role in this substorm onset, its coupling to the ion-scale processes is necessary to explain the wavelength of the onset waves.

2.1.3. THEMIS-D Observations: Distribution Functions

The directions of the ion and electron bulk velocities and energies of drifting populations can be confirmed by angle-resolved energy distributions shown in Figure 5. The 3-day distribution functions in this event were recorded every 96 s (except that the Solid State Detectors [SST] recorded ions every 3 s). Figures 5b–5d show ion dawn-dusk anisotropy. The ions above several keV were weakly directed duskward until ∼7 UT, and they correspond to the duskward ion velocity moment (Figure 4d). The duskward ion anisotropy was overall duskward and increased with energy, supporting that the duskward drift was related to the energy-dependent magnetic drift.

In Figures 5i–5k, the electron dawn-dusk anisotropy was variable, consistent with the small electron velocity moment in Figure 4e. When the electron velocity moment increased duskward around 06:53 UT, the plasma sheet electrons above several hundred keV had duskward anisotropy, confirming that the duskward velocity moment represents duskward drift of electrons.

Figures 5e–5g show the pitch angle anisotropy of the ions and electrons. Ions below a few keV and at tens of keV had field-aligned distributions before and soon after the onset. The field-aligned population largely contributes to the density moment at <1 keV (Figure 5a). Both low-energy (<1 keV) and plasma sheet (>1 keV) densities increased as the growth phase progressed. Throughout the time interval, the low-energy density remained comparable to the plasma sheet density, indicating that low-energy ions and plasma sheet ions had a nearly equal contribution to the plasma sheet density. Large contributions of low-energy ions during the growth phase have also been reported by Runov et al. (2021).

In Figure 5l–m, low-energy electrons were strongly field-aligned at most times, and the low-energy population can be seen as the enhanced fluxes in Figure 5l. Tens of keV electrons were also field-aligned during the growth phase, although their fluxes were low. Plasma sheet electrons at ∼1–10 keV energy were also weakly field-aligned initially, but then the perpendicular flux became larger prior to the onset at 06:40-06:50 UT. The electron density increased during the growth phase, and the low-energy electrons accounted for much of the density increase (Figure 5h), while the plasma sheet electron density was nearly constant during the growth phase. The contribution of the low-energy electron density to the total density increased from ∼40% at 06:00 UT to ∼70% soon before the onset. After the onset, the electrons mostly had field-aligned distributions, and the contribution of the low-energy density dropped substantially.

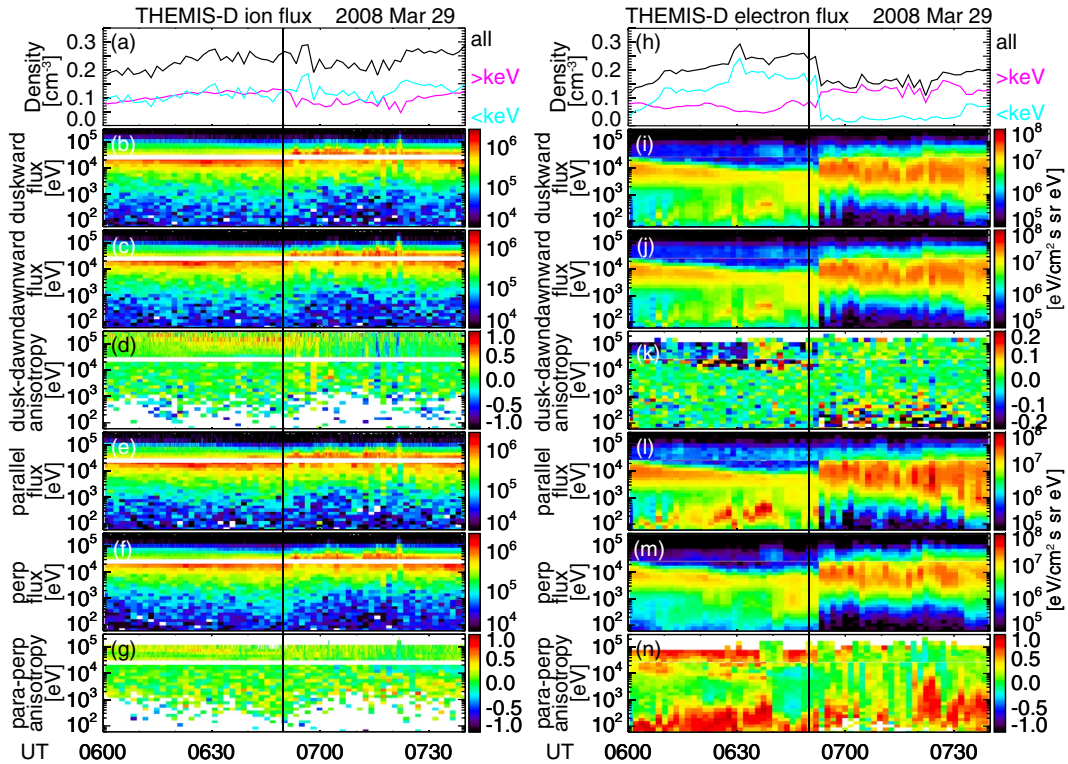

Figure 5. Density moments of (a) ions and (h) electrons. Energy spectrograms of (b) duskward ion fluxes (j_{dusk}), (c) dawnward ion fluxes (j_{dawn}), (d) dawn-dusk anisotropy (($j_{dusk} - j_{dawn}$)/($j_{dusk} + j_{dawn}$)), (e) field-aligned ion fluxes ($j_{||}$), (f) perpendicular ($j_{\perp}$) ion fluxes, and (g) pitch angle anisotropy (($j_{||} - j_{\perp}$)/($j_{||} + j_{\perp}$)) for Time History of Events and Macroscale Interactions During Substorms -D. Panels (i–n) are the same as Panels (b)–(g) except for electrons.

2.2. Eastward Propagation

2.2.1. Ground-Based and Multi-Satellite Observations

Figure 6 shows the second substorm event, which occurred on 20 November 2014. The preceding substorm was initiated at ~07:30 UT and moderate auroral activity above 65° MLAT continued until ~09:14 UT (Figure 6a). The auroral oval condition was nearly steady after ~08:20 UT without further electrojet enhancements. The equatorward portion of the auroral oval (<~65° MLAT) was quiet for more than 30 min before ~09:14 UT. Then a sudden auroral intensification occurred at 64° MLAT followed by a poleward expansion that reached the poleward boundary of the auroral oval. The auroral intensification was associated with a drop in the *H*-component of the ground magnetic field by ~270 nT (Figure 6b). The substantial poleward expansion and electrojet enhancements show that this is a substorm event. The substorm auroral onset was associated with clear auroral beads (onset waves) along the onset arc in the pre-midnight sector within the Fort Yukon (FYKN) imager FOV (Figure 6c). The footprints of THEMIS-A and E were within the MLT range of the onset waves, to the dusk of the emission peak of the onset arc. THEMIS-D was ~0.5 hr MLT duskward of THEMIS-E, and GOES-15 was at geosynchronous orbit ~2 hr MLT dawnward of THEMIS-A. The east-west keogram along the onset arc (Figure 6e) clearly shows that the auroral onset waves mainly propagated dawnward along the poleward-expanding bulge, in contrast to the duskward propagation in the first event. Weak pre-onset waves were seen to propagate duskward at 09:12-09:13:21 UT (small luminosity rise soon before the vertical line in Figure 6f), and then they were taken over by the onset waves. By referring to the longitude outside the pre-onset waves (blue line in Figure 6f), the auroral onset time was 09:13:21 UT, when the onset arc intensity started to increase exponentially.

Figures 6g and 6h show the cross-tail current and FAC that were derived from THEMIS-A, D, E, and GOES-15. The data from the individual satellites are shown in Figure S1 in Supporting Information S1. The currents peaked at 09:07 and 09:11 UT, and the growth phase arc intensity at −95.5° MLON (black line in Figure 6f) also peaked around the same times, indicating that the satellites and the growth phase arc were in the same current system.

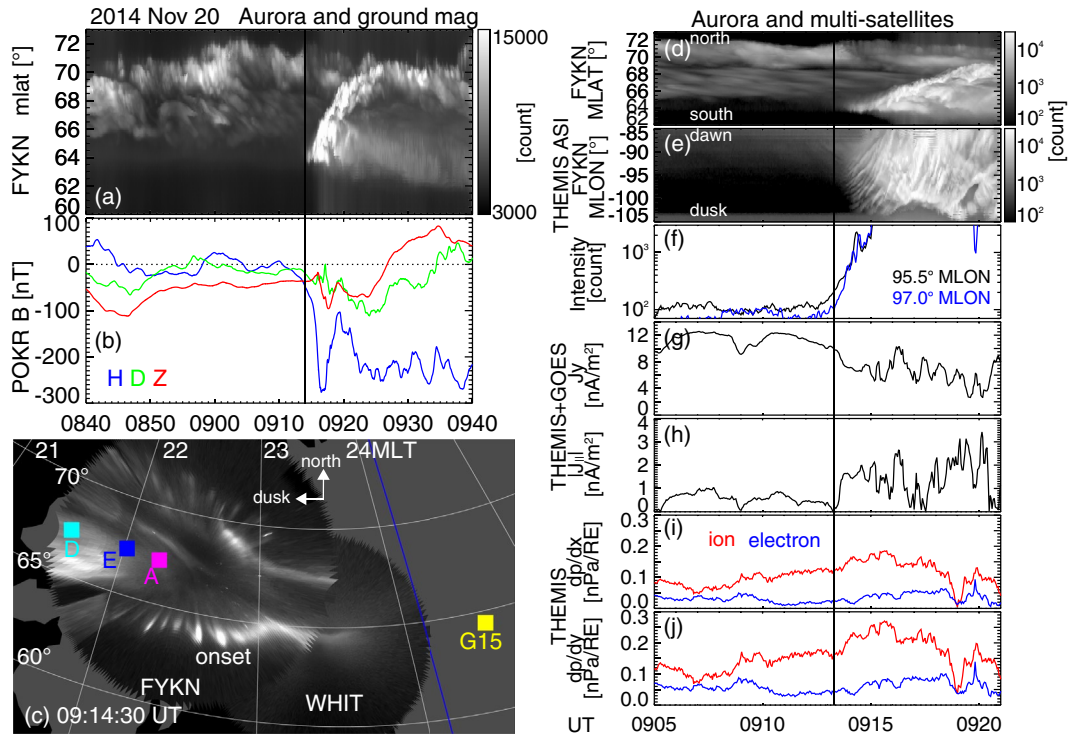

Figure 6. The left column shows (a) a north-south keogram from the Fort Yukon (FYKN) Time History of Events and Macroscale Interactions During Substorms (THEMIS) all sky imager (ASI), (b) ground magnetometer data at Poker Flat (POKR), (c) THEMIS ASI snapshot at 09:14:30 UT during the substorm on 20 November 2014. The right column shows (d) the north-south keogram from the FYKN ASI, (e) east-west keogram along the onset arc from the FYKN ASI (64.0° magnetic latitude), (f) line plots of auroral intensity on the onset arc (black: −95.5° and blue: −97.0° magnetic longitude), (g) duskward cross-tail tail current density and (h) field-aligned current density using the curlometer technique from THEMIS A, D, E, and GOES-15, and (i) sunward and (j) duskward pressure gradients (red: ion, blue: electron) from THEMIS A, D, and E.

After the auroral onset, the cross-tail current decreased and FAC increased. These changes are in agreement with the substorm current system, where a portion of the tail currents closes through the ionosphere as the auroral electrojet.

Similar to the previous event in Figure 1, the ion pressure gradient from THEMIS-A, D, and E was directed earthward and duskward, and it increased as the growth phase progressed. The ion pressure continued to increase until a few minutes after the substorm auroral onset and then decreased over time. Contrasting with the previous event in Figure 1, the electron pressure gradient was nearly parallel to the ion pressure gradient (earthward and duskward). The electron pressure was nearly steady during the growth phase and then slightly increased after the onset. The opposite direction of the electron pressure gradient to the previous event suggests that the role of electrons in this substorm was different from the previous event.

2.2.2. THEMIS-A Observations: Moments

We mainly examine observations by THEMIS-A, which was closest to the neutral sheet. THEMIS-A was in the central plasma sheet ($\beta = 2.1$ at 09:14 UT, Figure 7d) and crossed the neutral sheet soon after the substorm onset at 09:17-09:19 UT (B_x reversal in Figure 7c). β during the neutral sheet crossing (~20) was comparable to β in the previous event. B_z became negative for the first 2 min after the onset, and then started to increase (dipolarizations) after ~09:16 UT. Earthward BBFs were detected from 09:17 UT. After the onset, B_x and plasma velocities showed quasi-periodic oscillations of a ~30–60 s period, which was close to the period of the auroral onset waves (Figure 6b). The concurrent oscillations in both the ionosphere and plasma sheet suggest that the satellite was near the substorm onset region in the plasma sheet. The energy gap in the ion flux observations was large in this event (25–69 keV), and the ion thermal pressure and velocity moments lack contributions of the high-energy part of the plasma sheet population. Nevertheless, the total pressure during the growth phase was larger than that in the

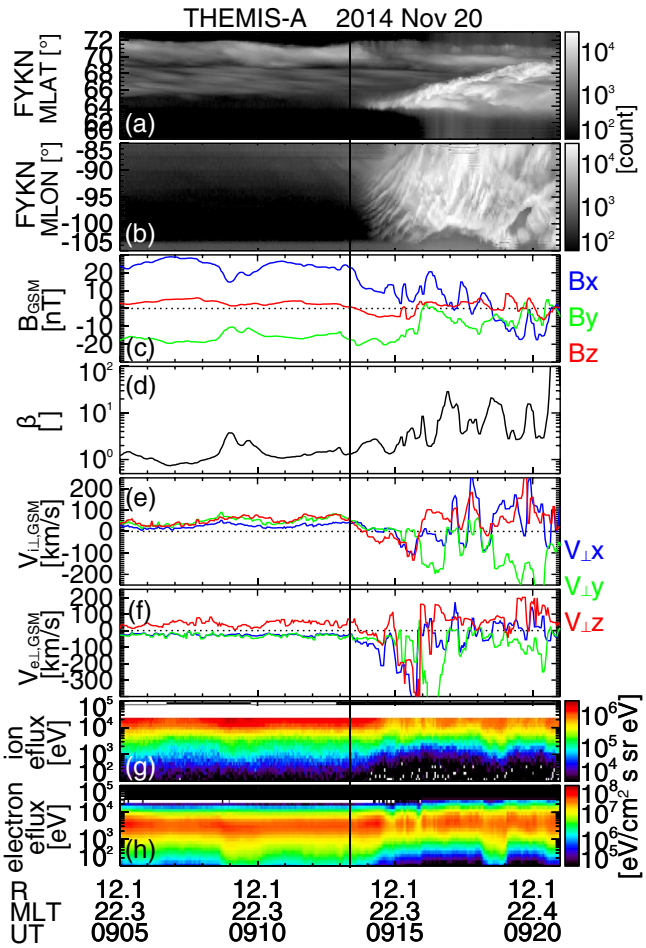

Figure 7. Same as Figure 2 but for Fort Yukon and Time History of Events and Macroscale Interactions During Substorms -A on 20 November 2014.

previous event (Figure S2 in Supporting Information S1). The electron density and ion temperature were also larger in this event despite that the satellite was away from the neutral sheet during the growth phase. These differences indicate that the loading in this event was stronger than that in the previous event, even though the two events had a similar level of the auroral electrojet strength during the expansion phase.

Another notable feature in Figure 7 is that v_x became temporarily negative at ~09:15 UT. This is not necessarily tailward plasma transport because v_z was also strongly negative. Considering positive B_x and negative B_z at this time, this plasma flow direction indicates equatorward plasma transport, which corresponds to earthward transport at the equator. The ion plasma flow during the neutral sheet crossing (09:17-09:19 UT) was indeed earthward.

A major difference from the previous event is the direction of the dawn-dusk plasma velocities. Figure 8c shows that the ion velocity before the onset was weakly duskward, and then it became nearly stagnant soon after the onset followed by a dawnward drift. The electron velocity was initially weakly dawnward, and then it increased dawnward after the onset. The dawnward electron velocity was comparable to the $E \times B$ velocity throughout this time interval. Thus the dawnward electron drift was due to the $E \times B$ drift. The dawnward ion drift was also likely affected by the $E \times B$ drift because magnetic drifts of ions were generally duskward. The dawnward $E \times B$ drift was associated with the equatorward electric field, where E_z was negative to the north of the neutral sheet ($B_x > 0$ before ~09:17 UT in Figure 7b) and positive to the south of the neutral sheet ($B_x < 0$ after ~09:17 UT). Equatorward E_z in the off-equatorial plasma sheet maps to earthward E_x at the neutral sheet. Earthward E_x was indeed observed during the neutral sheet crossing after 09:16 UT.

During the growth phase, both ion and electron currents were directed duskward, and the ion currents had a larger contribution to the net cross-tail current (Figure 8d). After 09:13:00 UT, the ion current decreased and then turned dawnward, while the electron current remained duskward with variable magnitudes. The electrons became the main carrier of the cross-tail current after the onset. This is a characteristic feature of the middle-tail current sheet (Lu et al., 2019; Runov et al., 2006). The strength of the net cross-tail current during the expansion phase was variable, but on average it became weaker than the current during the growth phase. The reduction of the cross-tail current at onset is consistent with the curlometer result in Figures 6g and 8 indicates that the current reduction is due to the reduction of the duskward ion drift under the equatorward (or earthward) electric field.

Figure 9 shows the ASI and satellite data in the same format as Figure 4. A 3-day distribution function data at THEMIS-A in this event do not have a sufficiently high time resolution to identify energy dependence of the drift speeds, and thus we evaluate the energy dependence using THEMIS-D data in the right column of Figure 9. THEMIS-D was 1 R_E earthward and 0.7 hr MLT duskward of THEMIS-A. β was ~0.2 and thus this satellite was farther away from the neutral sheet.

The dawnward ion and electron velocities, magnetic field, and pressures had quasi-periodic oscillations at ~30–60 s period at both satellites after ~09:13 UT. The auroral intensity along the onset arc also modulated at a similar period (Figure 9b), although the auroral waves did not have a one-to-one correspondence with the in-situ oscillations. The lack of one-to-one correspondence could be because of the difficulty of finding the mapping location under the time-varying magnetic field configuration. However, the simultaneous occurrence of the auroral and in-situ velocity oscillations suggests that the satellite detected in-situ signatures of the onset waves. The total pressure variations were dominated by the magnetic pressure oscillations, and the magnetic and plasma pressures were not balanced. The lack of the pressure balance may indicate that the oscillation involves substantial B_z oscillations on the equatorial plane as hinted by some B_z variations in Figure 9f. While B_x is generally balanced with

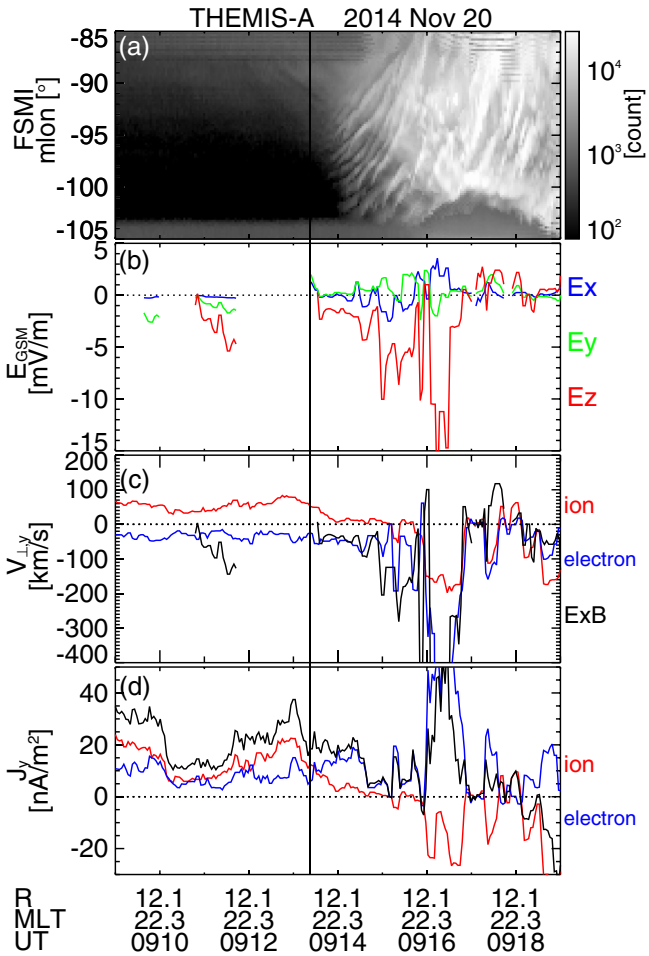

Figure 8. Same as Figure 3 except for Fort Yokun and Time History of Events and Macroscale Interactions During Substorms -A on 20 November 2014.

the thermal pressure in the z-direction, B_z does not contribute to this force balance and could change the total pressure. The ion and electron pressure variations were in-phase and had almost the same magnitudes.

The partial velocity moments from the distribution function data at THEMIS-D show that the velocities of the plasma sheet (>keV) and low-energy (<keV) populations were comparable to the total velocity moments. Both plasma sheet and low-energy ions drifted duskward during the growth phase, and then the velocities decreased and turned dawnward. The energy gap in the ion instruments was narrower than at THEMIS-A (Section 2.2.3), and the moments at THEMIS-D partially includes the high-energy part of the plasma-sheet ions. The electron velocities were nearly zero during the growth phase and then became overall dawnward after the onset. THEMIS-D also detected quasi-periodic oscillations of the electron velocity, magnetic field, and pressures. The pressure variations were dominated by the magnetic pressure, and the thermal pressure variations were anti-correlated with the magnetic pressure variations.

By tracing the structures of the onset waves in Figure 9a, the dawnward propagation velocity at 09:14-09:16 UT was found to be 2.5–8.6 km/s (0.05–0.18 deg/s) in the ionosphere. The velocity was not constant but increased over time (i.e., the slope of the onset wave in Figure 9a became steeper), giving the wide range of the velocity. This velocity range corresponded to 70–250 km/s dawnward velocity at the THEMIS location in the plasma sheet. This velocity range was comparable to both measured dawnward ion and electron velocities, but the electron velocity fell within the mapped velocity range for a longer time than the ion velocity. The ion velocity was still duskward in the first ~1.5 min from the onset. At THEMIS-D, the ion velocity did not reach the mapped velocity range, while the electron velocity reached the mapped velocity range. This comparison suggests that the dawnward propagation of the beads is likely related to the dawnward electron $E \times B$ drift. The wavelength in the ionosphere was ~39–54 km in the ionosphere or ~1,100–1,500 km in the plasma sheet.

Figure 10 examines phase relations of the quasi-periodic oscillations that were measured by THEMIS-A. The magnetic field and velocity in Figure 7 were smoothed over a 60-s window (Figures 10a and 10b). The smoothed data confirm that the neutral sheet crossing occurred at 09:18-09:19 UT, and that the velocity was mainly duskward. Band-pass filtered magnetic field and velocity in a 15–60 s window are shown in Figures 10c and 10d. The magnetic field quasi-periodic oscillation was predominantly in the B_x component, which is known as a flapping motion of the magnetotail (Sergeev et al., 2004). Kubyshkina et al. (2014) showed that kink and sausage modes in flapping oscillations can be distinguished by the sense of rotation of the plasma flow on the Y-Z plane. Figure 10e presents the phase angle of the ion velocity on the Y-Z plane. The phase angle tends to decrease in the northern hemisphere, while the angle tends to increase in the southern hemisphere. By referring to Figure 3 of Kubyshkina et al. (2014), these rotations in the dawnward velocity agree with the sausage mode (the kink mode has the opposite sense of rotation). In fact, the total pressure during the oscillations was not conserved but also modulated quasi-periodically. Thus the quasi-periodic oscillations can be considered as sausage-type flapping oscillations with periodic modulations of the total pressure, current sheet thickness, and plasma flows that propagated dawnward.

2.2.3. THEMIS-D Observations: Distribution Functions

Angle-resolved distribution functions by THEMIS-D are shown in Figure 11. The electron data have a gap of around 9 UT because of an operation mode change. The duskward ion fluxes were overall larger than the dawnward ion fluxes during the growth phase, while the dawnward ion fluxes became larger after the onset (Figures 11b–11d). Interestingly, plasma sheet ions at almost all energies drifted dawnward at ~09:18-09:23 UT. The ion dawnward drift across the wide energy range soon after the onset suggests that the duskward diamagnetic drift was not the most dominant component but the dawnward $E \times B$ drift likely became important for the ion drift

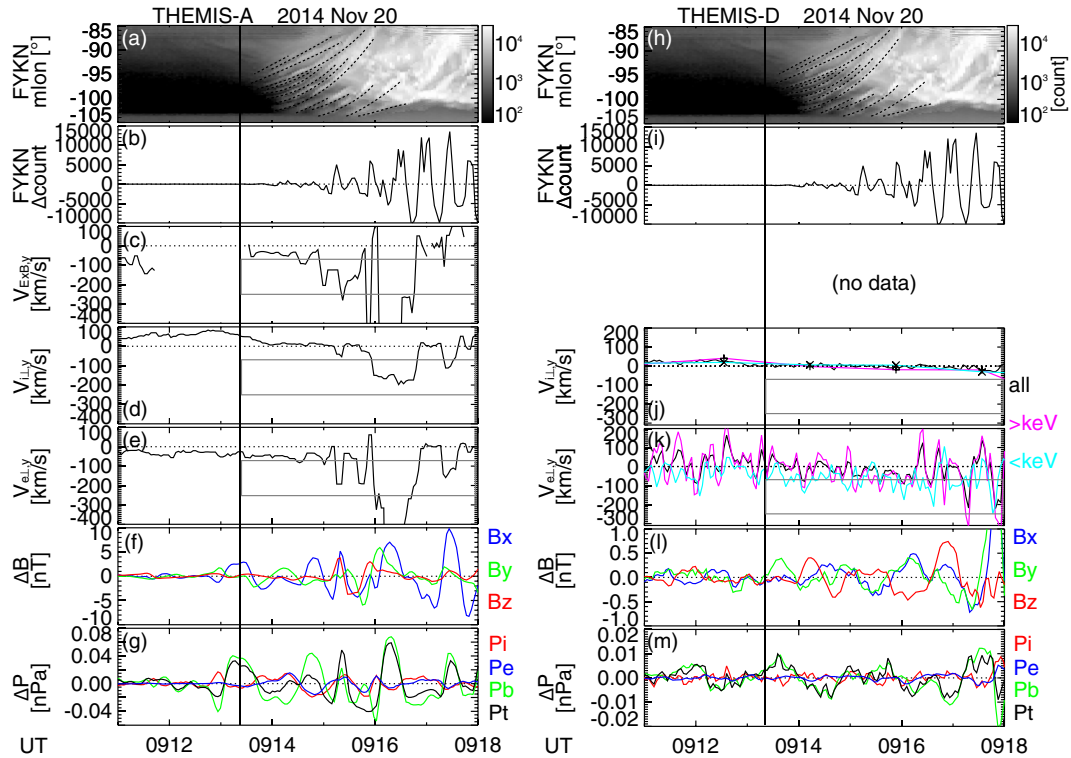

Figure 9. Same as Figure 4 except for the Fort Yokun all sky imager and (left) Time History of Events and Macroscale Interactions During Substorms (THEMIS)-A and (right) THEMIS-D on 20 November 2014. The 3-day distribution functions at THEMIS-A do not have sufficiently high time resolution. The $E \times B$ velocity at THEMIS-D is not available because the magnetic field is nearly on the spin plane.

motion. For electrons (Figures 11i–11k), the low-energy population below a few hundred eV predominantly drifted dawnward during the growth phase and early expansion phase until ~09:20 UT. The dawn-dusk anisotropy of the plasma sheet electrons at THEMIS-D was small and did not show a clear change at the onset.

The ions below ~1 keV and electrons below ~100 eV were highly field-aligned during the growth phase and soon after the onset (Figures 11e–11g and 11l–n). The presence of the field-aligned low-energy population is similar to the previous event and reiterates that outflowing plasma from the ionosphere substantially contributes to the plasma sheet density at substorm onset. The contribution of the low-energy plasma was smaller than in the previous event (<keV ions and <keV electrons had ~35 and ~45% of the total densities) but was not negligibly small.

3. Discussion

The present study focuses on examining the observed characteristics associated with the substorm onset waves, and we do not aim at determining the type of instability. Nevertheless, it is useful to discuss how the observed characteristics compare to existing theories. BICI (Pritchett & Coroniti, 2013) has been shown to reproduce observed wavelength and propagation velocity of onset waves (Nishimura et al., 2016). The duskward-propagation event in Section 2.1 also agrees with the BICI scenario, and thus BICI remains as a possible instability mode to create the onset waves. In the BICI mechanism, the dawnward wave propagation is caused by the dawnward $E \times B$ drift in the negatively charged current sheet. The negatively charged current sheet has been predicted theoretically (Hesse et al., 1998) and shown to form self-consistently (Lu et al., 2016, 2018; Pritchett & Coroniti, 1995). When the tail current sheet becomes thinner than that for the duskward-propagating bead event, ions are partially demagnetized and electrons are still magnetized. Such an ion-electron decoupling results in plasma polarization and formation of an electron-dominated current sheet with thin electron current layer embedded into thicker plasma density profile (Artemyev et al., 2009; Birn et al., 2004; Sitnov et al., 2006). The charge separation creates an equatorward and earthward electric field, where electrons drift dawnward by the $E \times B$ drift. In such a

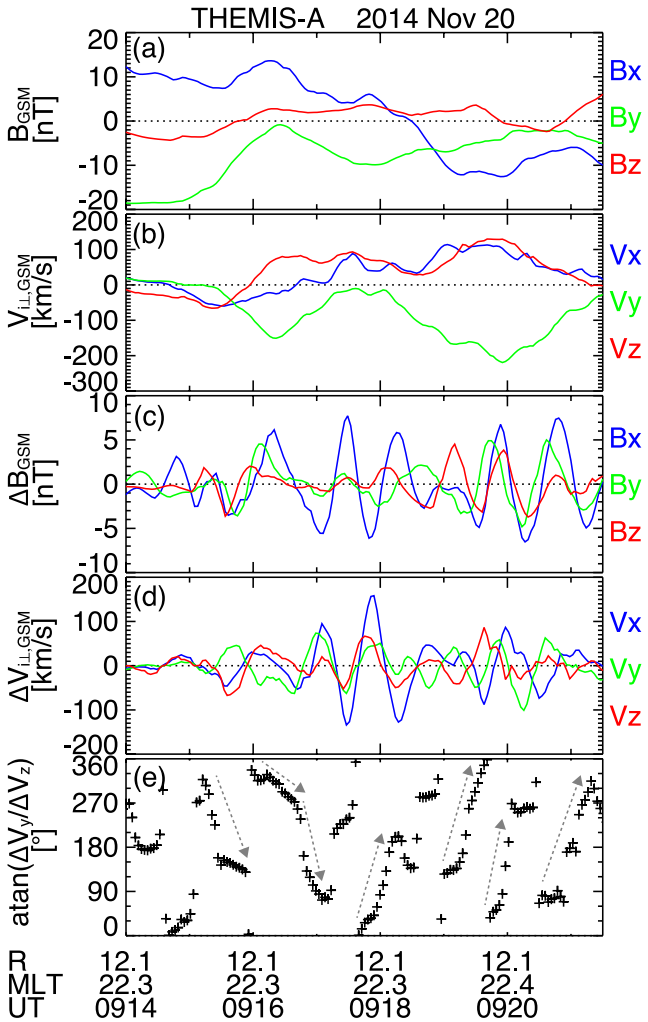

Figure 10. (a) Magnetic field and (b) $v_{i\perp}$ smoothed over 60 s. (c) Magnetic field and (d) $v_{i\perp}$ filtered in the 15–60 s window. (e) atan($\Delta v_{i\perp,y}/\Delta v_{i\perp,z}$) for the Time History of Events and Macroscale Interactions During Substorms -A data on 20 November 2014.

current sheet, the plasma flow is dominated by the $E \times B$ drift, whereas the spatial scale is still controlled by the ion Larmor radius scale. It is likely the scenario for the dawnward-propagation event in Section 2.2.

The analytical expression of the kinetic ballooning mode (Eq. 54 of Cheng [2004]) also showed that the ballooning mode depends not only on ions but also on electron drifts and electrostatic potential distribution. The present study provides observational evidence that the dawnward drifts of electrons (and low-energy ions) are indeed present during the dawnward-propagating onset waves. Cheng (2004) further discussed the role of electrons moving parallel to the magnetic field. The distribution function observations support that field-aligned distributions of electrons exist at low energies and their density is comparable to plasma sheet electrons.

Recently, global magnetohydrodynamic (MHD) simulations have been used to reproduce the bead structure (Raeder et al., 2010; Sorathia et al., 2020; Zhu & Raeder, 2014). Raeder et al., (2010) showed that the simulated waves have a ~0.5 R_E (~3,200 km) wavelength, which is within the range of the bead wavelength mapped to the equator (~1,100–3,600 km). Although Raeder et al. did not find a clear connection between the ballooning waves and substorm onset, the later work by Zhu and Raeder (2014) demonstrated its evolution to reconnection. Sorathia et al., (2020) also did not identify a connection between the MHD ballooning mode and substorm onset. The half size of their wave is ~4,000 km (i.e., ~8,000 km wavelength), and their wavelength is ~2–7 times larger than the beads. By closely examining the auroral observations on 15 February 2008 that Sorathia et al. (2008) investigated, the 'bead' structure is not associated with a substorm onset but a small intensification during a series of auroral activities. The MHD ballooning mode at a large wavelength may not represent waves at substorm onset but may be more applicable to other waves such as the ones during the growth phase (Panov et al., 2012).

In addition, the present observations have stressed the importance of the differential motion between ions and electrons for the development of the beads. Kinetic physics may be needed to cascade energy in the MHD ballooning scale down to the wavelengths comparable to the beads (~2,000–3,600 km). The MHD ballooning mode requires that the wave frequency is much lower than the ion gyrofrequency and that the wavelength is much longer than the ion gyroradius. Substorm onset beads do not satisfy these conditions because the wave frequency (~0.05 Hz) is close to the ion gyrofrequency (~0.1 Hz) and the wavelength (~2,000–3,600 km) is comparable to the ion gyroradius (~1,000 km). The drift ballooning instability (Pu et al., 1997) improves the treatment by considering diamagnetic and curvature drifts in anisotropic plasma, but the low-frequency and large-wavenumber assumptions are still required. The shear flow ballooning instability (Voronkov et al., 1997) considers an azimuthal flow at ~100 km/s, which is comparable to the observed $E \times B$ drift speed. While it is difficult to estimate the scale size of the flow shear observationally, the inclusion of the flow may explain the drift speed and direction of the instability.

The cross-field current instability (CCI) has been compared to observed bead properties and shown to reproduce the bead wavelength, period, and growth rate (Lui, 2020). In CCI, the wave propagation speed is duskward with respect to the electron drift speed. The waves propagate duskward when the electron drift speed is small, while the waves propagate dawnward in the inertial frame when the dawnward electron drift speed exceeds the wave propagation speed. The magnetic field, density, and temperature that were used in the instability analysis are comparable to the observations in our events (Figure S2 in Supporting Information S1), although their magnetic field and density are somewhat higher than the observations. CCI predicts a right-handed polarization, and it is consistent with the polarization seen in Figure 10 (the phase rotating from $+v_y$ to $+v_z$ axes in the northern hemisphere; from $+v_z$ to $+v_y$ axes in the southern hemisphere). One discrepancy, however, is the relative drift

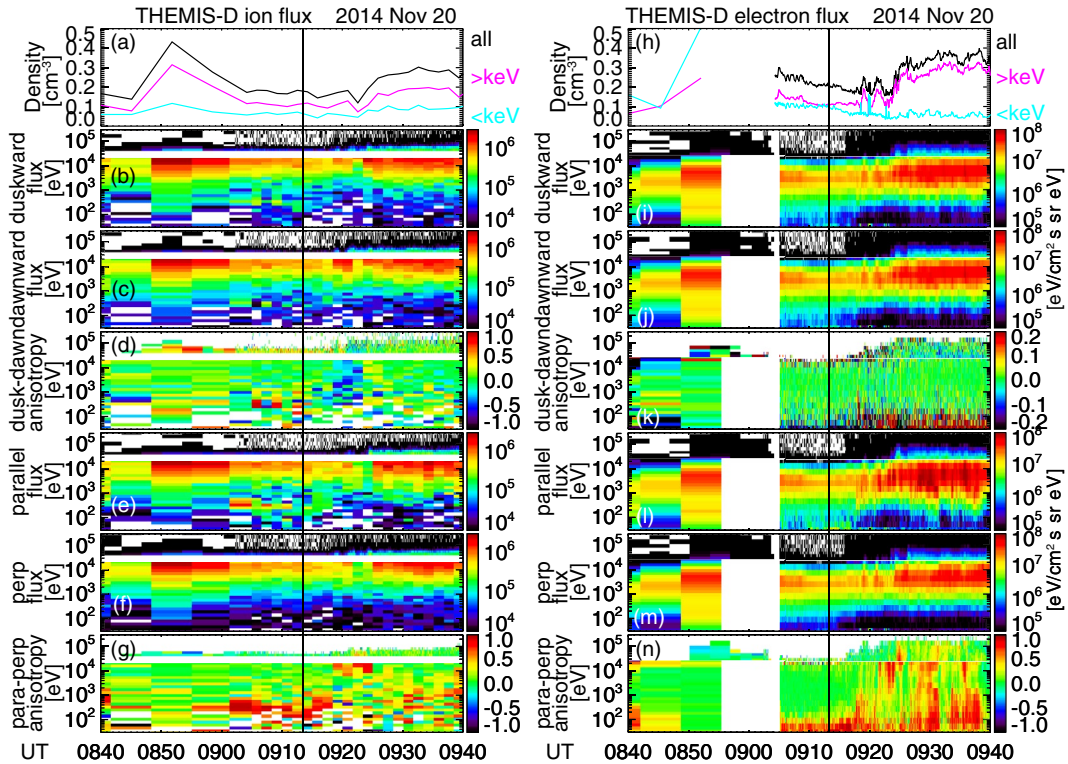

Figure 11. Same as Figure 5 except for Time History of Events and Macroscale Interactions During Substorms -D on 20 November 2014.

between ions and electrons (v_d). In Figures 6 and 7 of Lui (2020), v_d is required to be 0.02–0.04 v_e or 0.4–1.0 v_e, where v_e is the electron thermal speed. With ~1 keV electron temperature (Figure S2 in Supporting Information S1), v_d = 270–530 or 5,300–13,000 km/s. In Figures 3 and 8, the observed ion-electron velocity differences are ~50 km/s before the onset and ~0–200 km/s within a few minutes after the onset. Thus the observed speed difference is smaller than the relative drift speed required by CCI.

The current driven electromagnetic ion cyclotron instability (Perraut et al., 2000) predicts that onset waves are left-handed polarized, but it is inconsistent with the right-handed polarization of the observed polarization. Moreover, the fast magnetosonic mode expects that the magnetic and plasma pressure variations are in-phase, but the observations show the anti-phase relation (Figure 9) or did not show a clear phase relation (Figure 4).

4. Conclusion

We have examined plasma dynamics in the near-Earth plasma sheet that is associated with substorm onset beads using two substorm events with simultaneous THEMIS satellite and ASI observations. A particular emphasis was placed on identifying what plasma sheet features determine the duskward and dawnward propagating beads. The multi-satellite observations showed that the cross-tail current decreased and the FAC increased right at the substorm auroral onset. This current evolution at onset is consistent with the tail current diverting to the ionosphere and closing through the auroral electrojet. The earthward ion pressure gradient increased during the late growth phase and then decreased during the expansion phase, while the electron pressure gradient was nearly unchanged in the late growth phase.

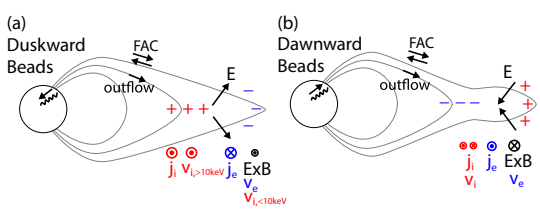

Figure 12. Schematic illustration of the magnetotail plasma, drift, current and electric field structures associated with the (a) duskward and (b) dawnward auroral beads.

The key magnetotail features for the duskward and dawnward bead events are summarized in Figure 12. In the duskward-propagating bead event, the electron pressure gradient was anti-parallel (tailward and dawnward) to the ion

pressure gradient (earthward and duskward). The electric field was outward (tailward and poleward), indicating that ions were accumulated to inner *L*-shells, while electrons were accumulated to outer *L*-shells. The tailward electric field corresponds to the duskward $E \times B$ drift, which was comparable to the duskward drift speed of electrons and was somewhat larger than the <10 keV ions. These drift speeds were small until a few minutes after the auroral onset, while the >10 keV ions drifted duskward throughout the event. The cross-tail current before the onset was carried by ions, but the cross-tail current became nearly zero in the first few minutes after the onset due to the increased speed of duskward drifting electrons. The reduction of the cross-tail current would weaken the magnetic field stretching in the magnetotail and may contribute to destabilizing the plasma sheet as an initiation of the substorm expansion phase.

In the dawnward-propagating bead event, the electric field was earthward (or equatorward at off-equatorial locations). The earthward electric field suggests that the electron current sheet is embedded to a thicker ion current sheet as predicted by kinetic simulations (Lu et al., 2018; Pritchett & Coroniti, 1995). The corresponding $E \times B$ drift was dawnward, and it was comparable to the dawnward electron drift speed. The ion drift was directed duskward in the growth phase and then turned dawnward after the onset. The electrons became the main carrier of the cross-tail current and the net current decreased soon after the onset, again indicating that the tail force balance changes at the onset. Lu et al. showed that the dawnward $E \times B$ drift enhances the thinning of the plasma sheet in the pre-midnight sector by removing the magnetic flux, while unmagnetized ions stay in the pre-midnight plasma sheet. The THEMIS data in this event provide an observational indication that the charged current sheet forms at substorm onset and plays a critical role in substorm onset instability. B_z briefly became negative at the satellite location after the onset. It is unclear if it is causally related to the onset process or not, but the negative B_z could be an indication of equatorial minimum-B and a magnetic field hump (Sitnov & Merkin, 2016).

The different orientations of the electric field in the two events suggest that the ion and electron distributions in the two substorms are substantially different, and that the differences in the electric field orientations distinguish the duskward and dawnward propagating onset waves. The two substorm events had a similar strength of the auroral electrojet, but the second event had a higher total pressure and ion temperature during the growth phase. The stronger magnetosphere driving in the second event would have contributed to form a thinner electron current sheet and the different electric field structure.

In the duskward-propagating bead event, the bead propagation speed (170–240 km/s in the tail) was close to the plasma sheet ion drift speed. The $E \times B$ and electron drift speeds also increased but not until a few minutes after the onset. In the dawnward-propagating bead event, the $E \times B$ and electron drift speeds were closer to the bead propagation speed (70–250 km in the tail) than the ion drift speeds. Thus we suggest that the plasma species that is responsible for the bead propagation changes with the electric field configuration in the magnetotail. The bead wavelength (2,000–3,600 and 1,100–1,500 km) was comparable to the gyroradii of plasma sheet ions, and thus ion kinetic effects are important for determining the wavelength. In the dawnward-propagating event, the mode of oscillation in the plasma sheet was suggested to be the sausage mode flapping oscillations.

Another important finding is the presence of the dense low-energy ions and electrons in the late growth phase. Their pitch angle distributions were mostly field-aligned, suggesting that a significant amount of plasma outflow from the ionosphere contributes to the plasma sheet density during the growth phase. The duskward $E \times B$ drift of electrons and the reduction of the cross-tail current at the substorm onset are largely contributed by the low-energy electrons. The dynamics of low-energy plasma should be considered in the plasma sheet force balance and substorm onset processes.

The present study emphasizes the importance of kinetic effects in the near-Earth plasma sheet for the substorm onset and auroral beads, and may provide crucial information for constraining the potential substorm onset mechanism. However, the results are based only on two conjunction events, and it is difficult to evaluate the results statistically because ideal conjunction events are extremely limited. Our work calls for further investigations of the near-Earth transition region from MHD to kinetic scales to fully understand the energy conversion process during substorms.

Data Availability Statement

The THEMIS data were obtained through themis.ssl.berkeley.edu. Data processing used SPEDAS-V3.1 (Angelopoulos et al., 2019).

Acknowledgments
This work was supported by NASA Grant 80NSSC18K0657, 80NSSC20K0604, 80NSSC20K0725, 80NSSC21K1321 and 80NSSC20K1788, NSF grant AGS-1907698 and AGS-2100975, and AFOSR grant FA9559-16-1-0364. We thank CEDAR for the "Grand Challenge: Multi scale I-T system dynamics" workshop, and ISSI/ISSI-BJ for the "Multi-Scale Magnetosphere-Ionosphere-Thermosphere Interaction" and "Magnetotail Dipolarizations: Archimedes Force or Ideal Collapse?" workshops. THEMIS is supported by NASA NAS5-02099 and Canada Foundation for Innovation.

References

Akasofu, S.-I. (1964). The development of the auroral substorm. *Planetary and Space Sciences*, *12*, 273–282. https://doi.org/10.1016/0032-0633(64)90151-5

Angelopoulos, V. (2008). *The THEMIS Mission* (p. 47). Space Sci. Rev.

Angelopoulos, V. (2019). The space physics environment data analysis system (SPEDAS). *Space Science Reviews*, *215*(1), 9. https://doi.org/10.1007/s11214-018-0576-4

Artemyev, A. V., Angelopoulos, V., Liu, J., & Runov, A. (2017). Electron currents supporting the near-Earth magnetotail during current sheet thinning. *Geophysical Research Letters*, *44*, 5–11. https://doi.org/10.1002/2016GL072011

Artemyev, A. V., Angelopoulos, V., Runov, A., & Petrokovich, A. A. (2016). Properties of current sheet thinning at x ∼− 10 to −12 RE. *Journal of Geophysical Research: Space Physics*, *121*, 6718–6731. https://doi.org/10.1002/2016ja022779

Artemyev, A. V., Angelopoulos, V., Runov, A., & Petrukovich, A. A. (2019). Global view of current sheet thinning: Plasma pressure gradients and large-scale currents. *Journal of Geophysical Research: Space Physics*, *124*, 264–278. https://doi.org/10.1029/2018ja026113

Artemyev, A. V., Angelopoulos, V., Runov, A., & Zelenyi, L. M. (2016). Earthward electric field and its reversal in the near-Earth current sheet. *Journal of Geophysical Research: Space Physics*, *121*, 10803–10812. https://doi.org/10.1002/2016JA023200

Artemyev, A. V., Petrukovich, A. A., Zelenyi, L. M., Nakamura, R., Malova, H. V., & Popov, V. Y. (2009). Thin embedded current sheets: Cluster observations of ion kinetic structure and analytical models. *Annales Geophysicae*, *27*(10), 4075–4087. https://doi.org/10.5194/angeo-27-4075-2009

Baumjohann, W., Paschmann, G., & Lühr, H. (1990). Pressure balance between lobe and plasma sheet. *Geophysical Research Letters*, *17*, 45–48. https://doi.org/10.1029/gl017i001p00045

Birn, J., Schindler, K., & Hesse, M. (2004). Thin electron current sheets and their relation to auroral potentials. *Journal of Geophysical Research*, *109*, A02217. https://doi.org/10.1029/2003JA010303

Boström, R. (1964). A model of the auroral electrojets. *Journal of Geophysical Research*, *69*(23), 4983–4999. https://doi.org/10.1029/JZ069i023p04983

Chang, T.-F., & Cheng, C.-Z. (2015). Relationship between wave-like auroral arcs and Pi2 disturbances in plasma sheet prior to substorm onset. *Earth Planets and Space*, *67*, 168. https://doi.org/10.1186/s40623-015-0334-8

Cheng, C. (2004). Physics of substorm growth phase, onset, and dipolarization. *Space Science Reviews*, *113*(1/2), 207–270. https://doi.org/10.1023/b:spac.0000042943.59976.0e

Donovan, E., Mende, S. B., Jackel, B., Syrjäsuo, M., Meurant, M., Voronkov, I., et al. (2006). The azimuthal evolution of the substorm expansive phase onset aurora. In M. Syrjäsuo, & E. Donovan (Eds.), *Proceedings of the Eighth International Conference on substorms* (pp. 55–60). Univ. of Calgary.

Dunlop, M. W., Balogh, A., Glassmeier, K.-H., & Robert, P. (2002). Four-point Cluster application of magnetic field analysis tools: The Curlometer. *Journal of Geophysical Research*, *107*(A11), 1384. https://doi.org/10.1029/2001JA005088

Gallardo-Lacourt, B., Nishimura, Y., Lyons, L. R., Ruohoniemi, J. M., Donovan, E., Angelopoulos, V., et al. (2014). Ionospheric flow structures associated with auroral beading at substorm auroral onset. *Journal of Geophysical Research: Space Physics*, *119*, 9150–9159. https://doi.org/10.1002/2014JA020298

Henderson, M. G. (2009). Observational evidence for an inside-out substorm onset scenario. *Annals of Geophysics*, *27*, 2129–2140. https://doi.org/10.5194/angeo-27-2129-2009

Hesse, M., Winske, D., & Birn, J. (1998). On the ion-scale structure of thin current sheets in the magnetotail. *Physica Scripta*, *63*. https://doi.org/10.1088/0031-8949/1998/t74/012

Kalmoni, N. M. E., Rae, I. J., Watt, C. E. J., Murphy, K. R., Samara, M., Michell, R. G., et al. (2018). A diagnosis of the plasma waves responsible for the explosive energy release of substorm onset. *Nature Communications*, *9*(1), 4806. https://doi.org/10.1038/s41467-018-07086-0

Kubyshkina, D. I., Sormakov, D. A., Sergeev, V. A., Semenov, V. S., Erkaev, N. V., Kubyshkin, I. V., et al. (2014). How to distinguish between kink and sausage modes in flapping oscillations? *Journal of Geophysical Research: Space Physics*, *119*, 3002–3015. https://doi.org/10.1002/2013JA019477

Le Contel, O., Perraut, S., Roux, A., Pellat, R., & Korth, A. (2000). Substorms in the inner plasma sheet. *Advances in Space Research*, *25*(12), 2395–2406. https://doi.org/10.1016/S0273-1177(99)00529-3

Liang, J., Donovan, E. F., Liu, W. W., Jackel, B., Syrjäsuo, M., Mende, S. B., et al. (2008). Intensification of preexisting auroral arc at substorm expansion phase onset: Wave-like disruption during the first tens of seconds. *Geophysical Research Letters*, *35*, L17S19. https://doi.org/10.1029/2008GL033666

Liu, J., Angelopoulos, V., Zhou, X.-Z., & Runov, A. (2014). Magnetic flux transport by dipolarizing flux bundles. *Journal of Geophysical Research: Space Physics*, *119*, 909–926. https://doi.org/10.1002/2013JA019395

Lu, S., Artemyev, A. V., Angelopoulos, V., Lin, Y., Zhang, X.-J., Liu, J., et al. (2019). The Hall electric field in Earth's magnetotail thin current sheet. *Journal of Geophysical Research: Space Physics*, *124*, 1052–1062. https://doi.org/10.1029/2018ja026202

Lu, S., Lin, Y., Angelopoulos, V., Artemyev, A. V., Pritchett, P. L., Lu, Q. M., & Wang, X. Y. (2016). Hall effect control of magnetotail dawn-dusk asymmetry: A three-dimensional global hybrid simulation. *Journal of Geophysical Research: Space Physics*, *121*, 11882–11895. https://doi.org/10.1002/2016ja023325

Lu, S., Pritchett, P. L., Angelopoulos, V., & Artemyev, A. V. (2018). formation of dawn-dusk asymmetry in Earth's magnetotail thin current sheet: A three-dimensional particle-in-cell simulation. *Journal of Geophysical Research: Space Physics*, *123*, 2801–2814. https://doi.org/10.1002/2017ja025095

Lui, A. T. Y. (1996). Current disruption in the Earth's magnetosphere: Observations and models, *Journal of Geophysical Research*, *101*(A6), 13067–13088. https://doi.org/10.1029/96JA00079

Lui, A. T. Y. (2020). Evaluation of the cross-field current instability as a substorm onset process with auroral bead properties. *Journal of Geophysical Research: Space Physics*, *125*, e2020JA027867. https://doi.org/10.1029/2020ja027867

Mende, S. B., Harris, S. E., Frey, H. U., Angelopoulos, V., Russell, C. T., Donovan, E., et al. (2008). The THEMIS array of ground-based observatories for the study of auroral substorms. *Space Science Reviews*, *141*, 357–387. https://doi.org/10.1007/s11214-008-9380-x

Miyashita, Y., Seki, K., Sakaguchi, K., Hiraki, Y., Nosé, M., Machida, S., et al. (2020). On the transition between the inner and outer plasma sheet in the Earth's magnetotail. *Journal of Geophysical Research: Space Physics*, *125*, e2019JA027561. https://doi.org/10.1029/2019ja027561

Motoba, T., Hosokawa, K., Kadokura, A., & Sato, N. (2012). Magnetic conjugacy of northern and southern auroral beads. *Geophysical Research Letters*, *39*, L08108. https://doi.org/10.1029/2012GL051599

Nishimura, Y., Lyons, L. R., Nicolls, M. J., Hampton, D. L., Michell, R., & Samara, M., et al. (2014). Coordinated ionospheric observations indicating coupling between preonset flow bursts and waves that lead to substorm onset. *Journal of Geophysical Research: Space Physics*, *119*, 3333–3344. https://doi.org/10.1002/2014JA019773

Nishimura, Y., Yang, J., Pritchett, P. L., Coroniti, F. V., Donovan, E. F., Lyons, L. R., et al. (2016). Statistical properties of substorm auroral onset beads/rays. *Journal of Geophysical Research: Space Physics*, *121*, 8661–8676. https://doi.org/10.1002/2016JA022801

Ohtani, S., Takahashi, K., Higuchi, T., Lui, A., Spence, H., & Fennell, J. (1998). AMPTE/CCE-SCATHA simultaneous observations of substorm-associated magnetic fluctuations. *Journal of Geophysical Research*, *103*, 4671–4682. https://doi.org/10.1029/97JA03239

Panov, E. V., Baumjohann, W., Nakamura, R., Pritchett, P. L., Weygand, J. M., & Kubyshkina, M. V. (2019). Ionospheric footprints of detached magnetotail interchange heads. *Geophysical Research Letters*, *46*, 7237–7247. https://doi.org/10.1029/2019gl083070

Panov, E. V., Sergeev, V. A., Pritchett, P. L., Coroniti, F. V., Nakamura, R., Baumjohann, W., et al. (2012). Observations of kinetic ballooning/interchange instability signatures in the magnetotail. *Geophysical Research Letters*, *39*, L08110. https://doi.org/10.1029/2012GL051668

Perraut, S., Le Contel, O., Roux, A., & Pedersen, A. (2000). Current-driven electromagnetic ion cyclotron instability at substorm onset. *Journal of Geophysical Research*, *105*(21), 97–107. https://doi.org/10.1029/2000JA900059

Petrukovich, A. A., Artemyev, A. V., Nakamura, R., Panov, E. V., & Baumjohann, W. (2013). Cluster observations of ∂Bz/∂x during growth phase magnetotail stretching intervals. *Journal of Geophysical Research: Space Physics*, *118*, 5720–5730. https://doi.org/10.1002/jgra.50550

Pritchett, P. L., & Coroniti, F. V. (1995). Formation of thin current sheets during plasma sheet convection. *Journal of Geophysical Research*, *100*(A12), 23551–23565. https://doi.org/10.1029/95JA02540

Pritchett, P. L., & Coroniti, F. V. (2013). Structure and consequences of the kinetic ballooning/interchange instability in the magnetotail. *Journal of Geophysical Research: Space Physics*, *118*, 146–159. https://doi.org/10.1029/2012JA018143

Pu, Z. Y., Korth, A., Chen, Z. X., Friedel, R. H. W., Zong, Q. G., Wang, X. M., et al. (1997). MHD drift ballooning instability near the inner edge of the near-Earth plasma sheet and its application to substorm onset. *Journal of Geophysical Research*, *102*(A7), 14397–14406. https://doi.org/10.1029/97JA00772

Rae, I. J., Watt, C. E. J., Mann, I. R., Murphy, K. R., Samson, J. C., Kabin, K., & Angelopoulos, V. (2010). Optical characterization of the growth and spatial structure of a substorm onset arc. *Journal of Geophysical Research*, *115*, A10222. https://doi.org/10.1029/2010JA015376

Raeder, J., Zhu, P., Ge, Y., & Siscoe, G. (2010). Open geospace general circulation model simulation of a substorm: Axial tail instability and ballooning mode preceding substorm onset. *Journal of Geophysical Research*, *115*, A00I16. https://doi.org/10.1029/2010JA015876

Roux, A., Perraut, S., Robert, P., Morane, A., Pedersen, A., Korth, A., et al. (1991). Plasma sheet instability related to the westward traveling surge. *Journal of Geophysical Research*, *96*(A10), 17697–17714. https://doi.org/10.1029/91JA01106

Runov, A., Angelopoulos, V., Artemyev, A. V., Weygand, J. M., Lu, S., Lin, Y., et al. (2021). Global and local processes of thin current sheet formation during substorm growth phase. *Journal of Atmospheric and Solar-Terrestrial Physics*, *220*, 105671. https://doi.org/10.1016/j.jastp.2021.105671

Runov, A., Sergeev, V. A., Nakamura, R., Baumjohann, W., Apatenkov, S., Asano, Y., et al. (2006). Local structure of the magnetotail current sheet: 2001 Cluster observations. *Annales Geophysicae*, *24*, 247–262. https://doi.org/10.5194/angeo-24-247-2006

Saito, M. H., Miyashita, Y., Fujimoto, M., Shinohara, I., Saito, Y., Liou, K., et al. (2008). Ballooning mode waves prior to substorm-associated dipolarizations: Geotail observations. *Geophysical Research Letters*, *35*, L07103. https://doi.org/10.1029/2008GL033269

Sakaguchi, K., Shiokawa, K., & Donovan, E. (2009). Azimuthal structures of ray auroras at the beginning of auroral substorms. *Geophysical Research Letters*, *36*, L23106. https://doi.org/10.1029/2009GL041252

Sergeev, V., Angelopoulos, V., Kubyshkina, M., Donovan, E., Zhou, X.-Z., Runov, A., et al. (2011). Substorm growth and expansion onset as observed with ideal ground-spacecraft THEMIS coverage. *Journal of Geophysical Research*, *116*, A00I26. https://doi.org/10.1029/2010JA015689

Sergeev, V., Runov, A., Baumjohann, W., Nakamura, R., Zhang, T. L., Balogh, A., et al. (2004). Orientation and propagation of current sheet oscillations. *Geophysical Research Letters*, *31*, L05807. https://doi.org/10.1029/2003GL019346

Shiokawa, K., Shinohara, I., Mukai, T., Hayakawa, H., & Cheng, C. Z. (2005). Magnetic field fluctuations during substorm-associated dipolarizations in the nightside plasma sheet around X = −10RE. *Journal of Geophysical Research*, *110*, A05212. https://doi.org/10.1029/2004JA010378

Sitnov, M. I., & Merkin, V. G. (2016). Generalized magnetotail equilibria: Effects of the dipole field, thin current sheets, and magnetic flux accumulation. *Journal of Geophysical Research: Space Physics*, *121*, 7664–7683. https://doi.org/10.1002/2016JA023001

Sitnov, M. I., Swisdak, M., Guzdar, P. N., & Runov, A. (2006). Structure and dynamics of a new class of thin current sheets. *Journal of Geophysical Research*, *111*, A08204. https://doi.org/10.1029/2005JA011517

Sorathia, K. A., Merkin, V. G., Panov, E. V., Zhang, B., Lyon, J. G., Garretson, J., et al. (2020). Ballooning-interchange instability in the near-Earth plasma sheet and auroral beads: Global magnetospheric modeling at the limit of the MHD approximation. *Geophysical Research Letters*, *47*, e2020GL088227. https://doi.org/10.1029/2020gl088227

Tsyganenko, N. A. (1995). Modeling the Earth's magnetospheric magnetic field confined within a realistic magnetopause. *Journal of Geophysical Research*, *100*, 5599–5612. https://doi.org/10.1029/94JA03193

Uritsky, V. M., Liang, J., Donovan, E., Spanswick, E., Knudsen, D., Liu, W., et al. (2009). Longitudinally propagating arc wave in the pre-onset optical aurora. *Geophysical Research Letters*, *36*, L21103. https://doi.org/10.1029/2009GL040777

Voronkov, I., Rankin, R., Frycz, P., Tikhonchuk, V. T., & Samson, J. C. (1997). Coupling of shear flow and pressure gradient instabilities. *Journal of Geophysical Research*, *102*(A5), 9639–9650. https://doi.org/10.1029/97ja00386

Wang, C.-P., Lyons, L. R., Nagai, T., & Samson, J. C. (2004). Midnight radial profiles of the quiet and growth-phase plasma sheet: The Geotail observations. *Journal of Geophysical Research*, *109*, A12201. https://doi.org/10.1029/2004JA010590

Yang, J., Wolf, R. A., Toffoletto, F. R., & Sazykin, S. (2013). RCM-E simulation of substorm growth phase arc associated with large-scale adiabatic convection. *Geophysical Research Letters*, *40*, 6017–6022. https://doi.org/10.1002/2013GL058253

Yue, C., Wang, C.-P., Nishimura, Y., Murphy, K. R., Xing, X., Lyons, L., et al. (2015). Empirical modeling of 3-D force-balanced plasma and magnetic field structures during substorm growth phase. *Journal of Geophysical Research: Space Physics*, *120*, 6496–6513. https://doi.org/10.1002/2015JA021226

Zelenyi, L. M., Artemyev, A. V., & Petrukovich, A. A. (2010). Earthward electric field in the magnetotail: Cluster observations and theoretical estimates. *Geophysical Research Letters*, *37*, L06105. https://doi.org/10.1029/2009GL042099

Zhu, P., & Raeder, J. (2014). Ballooning instability-induced plasmoid formation in near-Earth plasma sheet. *Journal of Geophysical Research: Space Physics*, *119*, 131–141. https://doi.org/10.1002/2013JA019511